

Spreading Dynamics of a Functionalized Polymer Latex

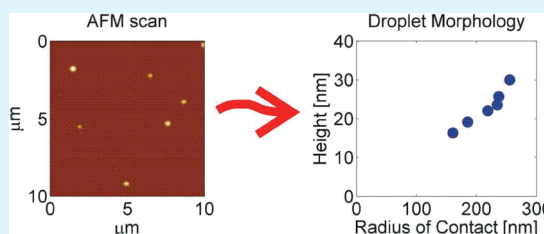
Jakob Kisbye Dreyer,* Tommy Nylander, Ola J. Karlsson, and Lennart Piculell

Physical Chemistry 1, Lund University, P.O. Box 124, SE-221 00 Lund, Sweden

S Supporting Information

ABSTRACT: Functionalized polymer nanoparticles are used as binders for inorganic materials in everyday technologies such as paper and coatings. However, the functionalization can give rise to two opposing effects: It can promote adhesion via specific interactions to the substrate, but a high degree of functionalization can also hamper spreading on substrates. Here, we studied the spreading kinetics of individual functionalized vinyl acetate-co-ethylene polymer nanoparticles on inorganic substrates by atomic force microscopy (AFM) imaging. We found that the kinetics underwent a transition from a fast initial regime to a slower regime. The transition was independent of functionalization of the particles but depended on the wettability of the substrate. Furthermore, the transition from the fast regime to the slow regime occurred at a size-dependent contact angle, leading to a $h \sim a^{3/2}$ scaling dependence between the height (h) and the width (a) of the spreading particles. Thereafter, spreading continued on a slower time scale. In the slow regime, the kinetics was blocked by a high degree of functionalization. We interpret the observations in terms of a nanoscale stick–slip transition occurring at interface stress around 6 kPa. We develop models that describe the scaling relations between the particle height and width on different substrates.

KEYWORDS: wetting, spreading, latex, nanoparticles, polymer, polymer melt, stick–slip, slippage, AFM friction, stationary friction



1. INTRODUCTION

Interactions between soft matter and hard surfaces are ubiquitous in nature as well as in technology. Often these interactions are modulated by specific molecules that promote adhesion. For example, the adhesion of cells to certain solid substrates often relies on specialized molecules located at the cell surface. Everyday technologies such as adhesives, inkjet printers, and coatings rely on interactions between polymer-based latexes and inorganic materials. Again, the adhesion may be optimized by the use of specific functional groups copolymerized into the polymer. In the present report, we investigate the role of such functional elements in a polymer system used in water-borne coatings.

In principle, water-borne coatings are applied as colloidal suspensions comprising a mixture of ~ 100 nm latex particles and inorganic ingredients such as fillers and pigments. The inorganic materials are typically calcium carbonate and titanium dioxide. During the drying process, the water evaporates from the suspension, which results in a coating where the polymer particles act as binders for the inorganic materials as well as to the substrate, onto which the coating is applied. In the dried coating film, the polymer is involved in interactions with (i) the coated surface, (ii) the inorganic particles (fillers), where the polymer adsorbs onto the surface of these compounds, and (iii) neighboring polymer particles, which fuse together to form a coherent film. So far, much research has been focused on the latter process, which has been investigated from a number of perspectives.^{1–3}

When the relative amount of inorganic constituents is low, the polymer particles are able to form a continuous matrix engulfing the filler material. However, with a high proportion of fillers, the mechanical and barrier properties of the applied film are mainly determined by interactions between the polymer particles and the inorganic materials.^{4,5} Thus, the ratio of binder and fillers determines the optimal type of polymer to maintain a coherent film.

When polymer particles are used as binders in coatings and adhesives, it is common to copolymerize functional monomers having certain chemical groups, such as, for example, methylol, silane, and epoxide functionalities. Coatings formulated with functionalized latexes are generally found to have lower water permeability and improved mechanical resistance, but a high degree of functionalization can lead to suboptimal coatings. The effect of functionalization is often attributed to specific chemical interactions between polymer and fillers, but functional groups may also lead to internal cross-linking of the particles.⁶ While this, on the one hand, may increase the mechanical resistance, it can also lead to low adhesion and formation of voids due to hampered film formation. Thus, the exact role of the functional groups is not well-known.

The scope of the present work is to elucidate the role of functionalization on the spreading of polymer nanoparticles onto inorganic substrates. In order to look into the basic physical principles, we investigated an idealized coating system in which

Received: August 20, 2010

Accepted: December 16, 2010

Published: January 19, 2011

single isolated polymer particles adhere to a flat inorganic surface. We then used atomic force microscopy (AFM) imaging to follow spreading of the particles. This method was first used by Granier and Sartre,⁷ who demonstrated the use of AFM in studies of latex adhesion. Later, Unertl⁴ used AFM to measure the contact angle of styrene–butadiene polymer particles and thereby calculated the work of adhesion using the Young–Dupree formula. Extending this work Lau et al.^{8,9} included the mechanical stress of the droplets in a model that enabled calculation of the adhesive energy of latex particles with different elastic properties. However, Engqvist et al. have recently shown that when the polymer elasticity was included in the Young–Dupree equation, the work of adhesion for large and glassy latex particles differed largely compared to earlier studies.¹⁰

In our study, we investigated the relationship between the height and width of more than 700 polymer droplets incubated under different conditions and on different surfaces. We found that spreading proceeded via a fast initial phase followed by a slow phase. The crossover between the fast and slow phases occurred at a specific contact angle depending on the particle size. However, in spite of the different rheological properties of the latexes, the crossover did not depend on functionalization of the particle. In this respect, only the further long-time development of the morphology of the particles was dependent on functionalization. At long times, the shape of highly functionalized particles did not evolve at all, whereas nonfunctionalized particles evolved in a nonlinear manner. On time scales relevant for coating applications, the particles did not reach thermodynamic equilibrium.

On the basis of these observations, we propose that spreading of polymer nanodroplets proceeds by a stick–slip mechanism. Initially, the droplets spread fast because polymers at the interface slip. Slippage stops when the stress at the interface falls below the critical level for a stick–slip transition. Thereafter, spreading continues on a slower time scale. We believe that the slow phase corresponds to a situation where relaxation of the internal stress enables parts of the interface to slip. The stick–slip model is consistent with observed scaling relations between the height and width, and estimates of the critical stress at the stick–slip transition are comparable to those from previous macroscopic studies.

Because the stick–slip model only involves the film height and degree of polymerization, we believe this to be a common mode of spreading for nanoscale polymer particles at low contact angles.

2. EXPERIMENTAL SECTION

2.1. Latexes. Three types of latexes with varying degrees of functionalization were studied. We denote by F_0 as a nonfunctionalized latex, whereas F_1 is a medium-functionalized latex and F_2 denotes the highest degree of functionalization. The nonfunctionalized latex is a statistical copolymer consisting of vinyl acetate (85 wt %, i.e., 66 mol %) copolymerized with ethylene (PVAE). In the functionalized particles, a fraction of the monomers were randomly copolymerized with vinylsilane and an epoxide containing acrylic (from 0.1% to 2%; see precise values in Table 1) in order to emulate a typical coating application. The particles are shown schematically in Figure 1. Details regarding the functional monomers are given in ref 11. Silane and epoxide functionality provides several possible reaction pathways that will result in cross-linking of the polymer and/or reaction with a substrate; e.g., silane groups can undergo hydrolysis followed by a subsequent condensation reaction to form polymer cross-links or a substrate coupling with a silica surface. The epoxide group is a versatile functionality that provides a variety of paths, and common cross-linking and coupling reactions involve active hydrogen atoms.¹²

Table 1. Properties of Latexes Used in the Study^a

particle	silane (pphm ^b)	epoxide (pphm)	VAD, light scattering (nm)	VAD, AFM (nm)	T_g (°C)
F_0	0	0	1.4×10^2	143 ($N = 320$)	8
F_1	0.2	1	1.3×10^2	138 ($N = 106$)	6
F_2	0.4	2	1.3×10^2	135 ($N = 283$)	7

^a The volume-averaged diameter (VAD) was determined by light scattering and calculated using data from the AFM scans using eq 2.

^b pphm = parts per hundred monomers.

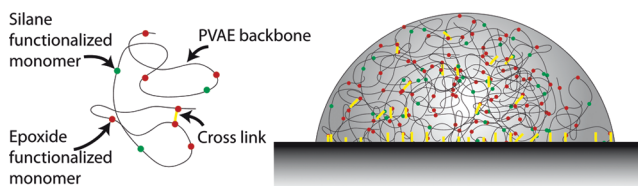


Figure 1. Schematic illustration of functionalized polymer particles. Left: The base polymer is PVAE. A small fraction of monomers containing functional silane and epoxide groups are schematically shown as red and green dots (nonfunctionalized monomers are not shown). An inter-monomer cross-link is shown in yellow. Right: Functionalized particle on a substrate. Putative interactions are shown in yellow: both internal cross-links and specific interactions with the substrate may form.

The average sizes of the latex particles, the amounts of the functional groups, and the glass temperatures T_g are given in Table 1. Particle size distributions were measured using light scattering (Malvern Mastersizer 2000) and are shown in the Supporting Information.

The latex particles used in the present study were noncommercial samples prepared in a pressurized emulsion polymerization process by Celanese Emulsions Norden AB, Perstorp, Sweden. All of the polymerizations were performed in a 5 L calorimetric pressure reactor (Chemisens AB, Lund, Sweden) at 65 °C at 33 bar pressure using the same procedure and basic recipe. The reactor was first filled with a mixture of water, equal amounts of anionic and nonionic surfactants, and a reducing agent as part of a redox initiator system. A total of 5% of the total amount of liquid monomers (i.e., vinyl acetate, vinylsilane, and epoxide monomer) was charged to the reactor, and the ethylene pressure was held at 15 bar before the reaction was started by the redox initiating system with the addition of an oxidizing agent. After the precharge had reacted, forming particle nuclei, the remaining monomers were fed to the reactor for 300 min and the pressure was increased to 33 bar. After the polymerization reactions were finished, the dispersions were filtered and the residual monomer was further reduced by chemical post-treatment.

The polymerization rate was measured and monitored using the reaction calorimeter online to allow precise control of the polymer composition and final particle size. The semicontinuous addition of monomers, using a slow feed to obtain monomer-starved conditions, prevented compositional drift during copolymerization. In monomer-starved copolymerization reactions, there is less possibility of building up an excess of one of the monomers because the monomers are consumed as they are charged to the reactor.¹³ This results in a homogeneous overall copolymer composition with an even distribution of functional monomer throughout the particles.

Surfactants, oligomers, initiator residuals, etc., stemming from the emulsion polymerization of the particles were removed by dialysis using deionized water. Here, the dialysis tubes (Spectrapor, MwCo 100k) filled with suspensions of particles were kept in deionized water for at least 10 days, with the water being continuously renewed. In order to

facilitate observation of isolated particles, the dialyzed latex dispersions were diluted by a factor of 10^4 .

2.2. Creep Measurement. The rheology of macroscopic films of the polymer latexes was investigated in parallel-plate geometry (AR2000-rheometer, TA Instruments). The films were formed using the undialyzed latex dispersions, which were poured into Petri dishes to form 1–2-mm-thick layers. After evaporation of the water, the films were annealed for 4 days at 80 °C. The final films were cut into 25-mm-wide disks, which were inserted into the rheometer. The film thickness was approximately 200 μm . Prior to each creep experiment, a strain sweep was performed in order to confirm linear viscoelasticity. The initial strain was selected to be in the regime of linear viscoelasticity. The temperature during the experiment was 80 °C.

2.3. Surfaces. The untreated surfaces were silicon wafers with a thermally grown SiO_2 layer of 300 Å thickness. These were cleaned by boiling in a solution of 160 mL of Milli-Q water, 30 mL of H_2O_2 , and 30 mL of NH_3 for 5 min. After they were washed with Milli-Q water, the wafers were boiled in a solution of 160 mL of Milli-Q water, 30 mL of H_2O_2 , and 30 mL of HCl for 10 min. Finally, the plates were washed by copious amounts of Milli-Q water.

Dimethyloctylchlorosilane (Me2-OdCS)-modified surfaces were prepared by gas-phase silanization; for an extensive discussion of silanization of silicon wafers, see ref 14. The wafers were first cleaned as described above, then dried under vacuum (0.001 mbar), and treated in a plasma cleaner (Harrick Scientific Corp., model PDC-3XG) for 5 min. They were then immediately placed in a 2 L desiccator with about 2 mL of dimethyloctyldichlorosilane (Lancaster Synthesis Ltd.), and the desiccator was evacuated for 20 min by means of a vacuum suction pump (15–20 mbar), after which the valve to the vacuum was closed. The silicon wafers were then exposed to Me2-OdCS vapor for another 30 min under a vacuum. Then the Me2-OdCS-modified surfaces were sonicated for 20 min in three cycles: first in tetrahydrofuran, then in ethanol, and finally in ethanol. The Me2-OdCS treatment gave mildly hydrophobic surfaces with a water contact angle of $55 \pm 2^\circ$, using 5 μL of Milli-Q water droplets (results from 5 drops each on two different surfaces). The Me2-OdCS-modified surfaces used were prepared as a single batch. All surfaces were kept submerged in ethanol until use, and all were used within a time span of 4 months from the preparation, although these types of surfaces were found to be stable for at least 1 year. In the AFM measurements, the Me2-OdCS film was uniform and 3–4 nm thick (see Figure 2 in the Supporting Information).

Spreading of the latex particles on surfaces with a higher degree of hydrophobicity was also examined. However, on such surfaces, isolated particles could not be uniquely identified.

2.4. Sample Preparation. A total of 1 drop of dialyzed polymer dispersion diluted in water was placed on the silicon wafer. After the initial evaporation of water at ambient conditions, the dried particle dispersion formed a ringlike pattern, similar to a coffee stain, due to convection currents during drying.¹⁵ The sample was incubated at $T = 80^\circ\text{C}$, except where indicated. The incubation time was varied from 1 to 24 h. After incubation, the sample was cooled in a Petri dish under ambient conditions. The cooling time was on the order of minutes. Regions with a suitable density of isolated particles could be found near the inside of the ring of the dried dispersion. These particles were characterized by AFM. In some measurements, the sample was reheated to investigate the continued spreading of the same sample at different incubation times.

2.5. AFM Measurement. The samples were investigated under ambient conditions using tapping-mode AFM (Nanoscope 3, Digital Instruments, Santa Barbara, CA). Images of $10\ \mu\text{m} \times 10\ \mu\text{m}$ were recorded with a line scan rate of 1–2 Hz. The amplitude setpoint for the feedback loop was 50% of the free oscillation amplitude. Cantilevers were of type RTESP (Veeco probes). Tip corrections were not applied because the radius of curvature of the spread latex particles was much larger than that of the AFM tips.

We verified that the AFM measurements did not affect the shape of the particles by repeated measurements (see Figure 3 in the Supporting Information) and by determination of the average particle size from the AFM data (see below). The setup was calibrated using grids (TGZ02, Micromarsh; see the Supporting Information).

2.6. Data Analysis. The shape of the particles was extracted from the raw data of the AFM scans in a procedure that included several steps. The first step selected particles for further analyses as isolated regions with an elevation of more than 5 nm above the background (this threshold was lowered to 3 nm for the most spreading particles, F_0 particles incubated for 24 h). The threshold was chosen to detect isolated particles, and it was verified that all particles were detected. The selection process was made by a software algorithm in *Matlab* to ensure an unbiased choice of particles for analysis. In order to reduce the number of false positives, the selection was carried out on a smoothed copy of the original image. Physical data from the particles were extracted directly from recorded data without any smoothing.

The particle detection algorithm could not automatically distinguish isolated particles from agglomerates or imaging artifacts. Therefore, the integrity of all particles selected for further analyses was verified manually. For this study, a total number of 1108 particle candidates was examined from 30 different AFM scans. Of these, 132 particles were discarded, being either artifacts (typically 1–2 pixels wide spots) or particles only partially in view in the image. Of the remaining 976 potential particles, 271 were identified as agglomerates of several particles or being too close to neighboring particles.

Once an isolated particle was identified, the AFM scan line that included the center of mass of the particle was extracted from the raw unprocessed AFM scan. The cross section was always taken in the x direction (the scan direction) of the scanned image. The background was subtracted from the scan line using a linear fit to the data points not belonging to the peak. It was visually verified that the background was correctly detected. We determined the standard deviation of the baseline as an estimate of the noise level in the AFM measurement.

We parametrized the spreading particles by the contact radius and maximum height. These quantities can be extracted in several ways. Here we used two methods. The first is a simple measurement of the maximum height of the particle as the peak value of the cross section of the particle. We defined the width as the length of the cross section where all data points were more than 1 standard deviation above the background. In the second method, we approximated the shape of the particle by a spherical cap and extracted the height and width using a curve fit. The spherical cap function used for the fit is defined as

$$\eta(x) = \begin{cases} \sqrt{R^2 - (x - x_0)^2} + h - R & \text{for } x - x_0 \leq a \\ 0 & \text{for } x - x_0 > a \end{cases} \quad (1)$$

where x is the coordinate along the cross section, $a = (2hR - h^2)^{1/2}$ is the contact radius of the droplet, R is the radius of curvature, and x_0 is the center coordinate. From these parameters, the contact angle θ is calculated as $\sin(\theta) = 2ha/(a^2 + h^2)$.

The simple procedure is more conservative than the spherical cap fit in the sense that there are no assumptions regarding the particle shape. However, more precise values, which gave less scatter of the data, were obtained by fitting the spherical cap function to the data.

An example of the results from our AFM measurement method is shown in Figure 2. Here, panel A shows raw data obtained from a typical $10\ \mu\text{m} \times 10\ \mu\text{m}$ AFM scan. The polymer particles appear as circular bright regions. Typically, the images contained an ensemble of particles of different sizes. Figure 2B shows the cross section of one of the particles in panel A (indicated by a line in Figure 2A). Using conservative estimates, the contact radius of the particle was found to be 283 nm and the maximum

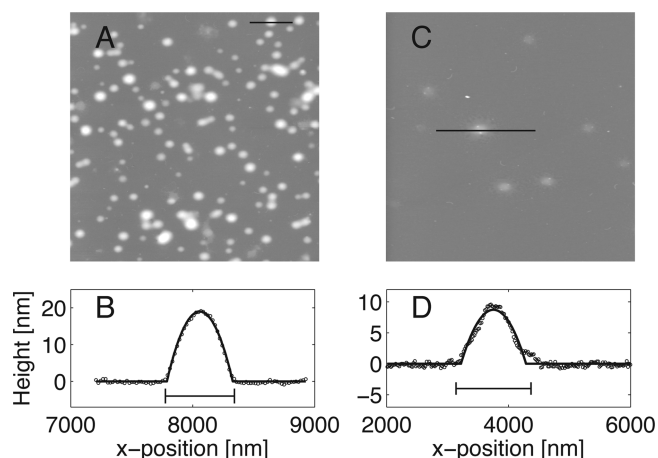


Figure 2. Example of AFM measurement and extraction of the physical parameters of the spreading drops. Panel A: $10\ \mu\text{m} \times 10\ \mu\text{m}$ AFM image for F_1 incubated 24 h on Me2-OdCS-modified silicon. Panel B: Cross section of a particle from panel A. The bar indicates the 566 nm diameter of the particle. The maximum height of the particle was 19 nm. Using the spherical cap fit (solid line), we obtained $a = 270 \pm 2.5\ \text{nm}$ and $h = 19.0 \pm 0.2\ \text{nm}$. The line segment used in panel B is indicated in panel A as a black line. Note that the x and y axes in panel B do not have the same scale. Panel C: Same as panel A but with F_0 particles incubated 24 h on untreated silicon. Panel D: Cross section of a particle from panel C. The scale bar indicates the diameter of the particle (1200 nm). The height of the particle was 9 nm. The solid line indicates a fit of a spherical cap function to the cross section. See the note on calibration in the Supporting Information.

height was 19 nm. Using the spherical cap fit, we obtained $a = 270 \pm 2.5\ \text{nm}$ and $h = 19.0 \pm 0.2\ \text{nm}$.

In the majority of the cases, we found good agreement between the two ways of measuring the particle size. An example of particles for which some difference could be observed is shown in Figure 2C,D. Here, the cross section revealed deviations from the spherical cap shape and indications of 1–2-nm-thick precursor films¹⁶ (Figure 2D). Also, the spherical cap fit tended to underestimate the maximum height and width. Such deviations were more frequently encountered after long incubation times on untreated surfaces compared to Me2-OdCS-modified surfaces.

In order to rule out the possibility of systematic errors induced by a particular model, we therefore made a survey of the relative differences between the measured peak height and the fitted value h for all particles observed on the untreated surfaces. The results are shown in Figure 3, where also the particle of Figure 2D is indicated by a circle. The study indicated that the spherical cap fit tended to be less accurate for the particles that spread the most (having low heights and relatively large contact radii). Here the spherical cap fit underestimated the peak height by up to 15%, whereas deviations were low for the majority of the particles that spread less. However, the morphological difference between the highly spreading particles and the others was larger than what could be accounted for by inaccurate modeling. We therefore exclusively used the fitted parameters to describe the droplet morphology in the study.

We then checked whether indentation artifacts influenced our measurements. Indentation of the AFM tip will cause the height of the particles to be systematically underestimated. In order to test for this we compared the calculated volume of the spherical cap data with the original size of the particles as measured by light scattering. Thereby, we compared the size of the spreading particles on the substrate with a noncontact measurement of the particles in solution. The volume was calculated as

$$\Omega = \frac{1}{6}\pi h(3a^2 + h^2) \quad (2)$$

In order to facilitate comparison with the light scattering data, we calculated the volume-averaged diameter (VAD) for each batch of particles

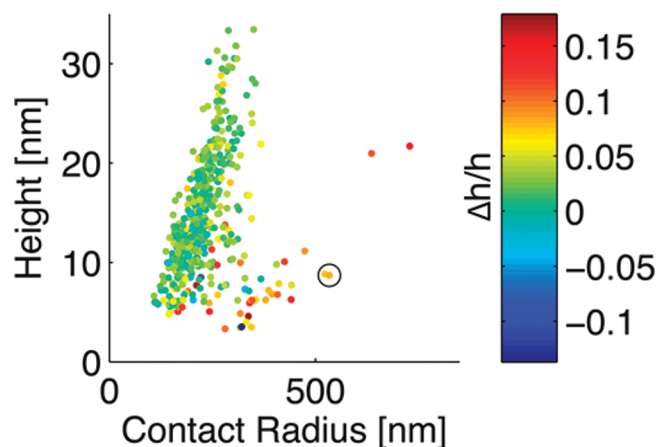


Figure 3. Relative difference between the height from a spherical cap fit and the measured maximum value for particles of all functionalities on untreated silicon. Each dot represents the contact radius and height of a particle. Color indicates the relative difference between h from the spherical cap fit and the maximum height of the cross section. The particle shown in Figure 2D is highlighted by a black circle.

(data given in Table 1). The agreement between diameters was very good, showing that indentation errors induced by the AFM measurement were low.

Data analysis was carried out in *Matlab*, version 7.6, including the Curvefitting and Statistics Toolboxes.

3. RESULTS

The various functionalized polymers used in this study (Table 1) are similar to latexes used in coatings. The aim with the functionalization is to enhance the durability of the coating, but it is often observed that too much or too little polymer modification deteriorates the end product. In this study, we investigated the effect of these changes in a model system. Functionalization of the polymer will affect both the adhesive and cohesive properties of a film. For example, the introduced silane groups are expected to readily react with the siloxane groups on the silicon oxide surface.¹⁴

The most direct measurement of the cohesive strength of the polymer film is creep measurements. Here the film was subjected to a constant stress, and we measured the strain as a function of time. Our results from this experiment are shown in Figure 4. Circles represent a film formed by the nonfunctionalized latex, F_0 . For this film, we observed a constantly increasing strain, indicating that the film had liquidlike behavior. The slight upward curvature indicates shear thinning. From these data, the viscosity at $80\ ^\circ\text{C}$ was determined from the strain rate to be $\eta \sim 2.9 \times 10^4\ \text{Pa s}$, corresponding to $\eta \sim 10^7\ \text{Pa s}$ at $25\ ^\circ\text{C}$.¹⁷ Data points of the intermediately functionalized latex, F_1 , are indicated by squares. Here, the strain rate was lower and appeared to decrease at long times, which is a signature of a cross-linked polymer. Finally, asterisks represent the highly functionalized latex, F_2 . Here, the strain became constant on a time scale of minutes, indicating that the high density of cross-links in the polymer gave the film rubberlike properties on this time scale.

3.1. Functionalization of Latex Prevents Spreading on a Silicon Substrate. We then asked what is the effect of functionalization for interaction with a model inorganic substrate. Changes in the polymer chemistry of the drops will be reflected in different spreading behavior. To this end, we incubated particles of different functionality for 24 h at $80\ ^\circ\text{C}$ on untreated silicon surfaces and measured the height and width of the particles using AFM.

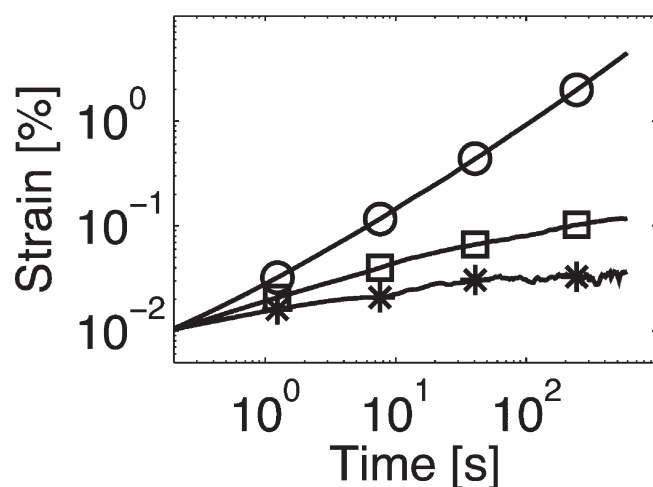


Figure 4. Creep experiment on the macroscopic latex film at $T = 80\text{ }^{\circ}\text{C}$. The figure shows the strain at constant stress as a function of time. Circles indicate F_0 , squares F_1 , and asterisks F_2 particles.

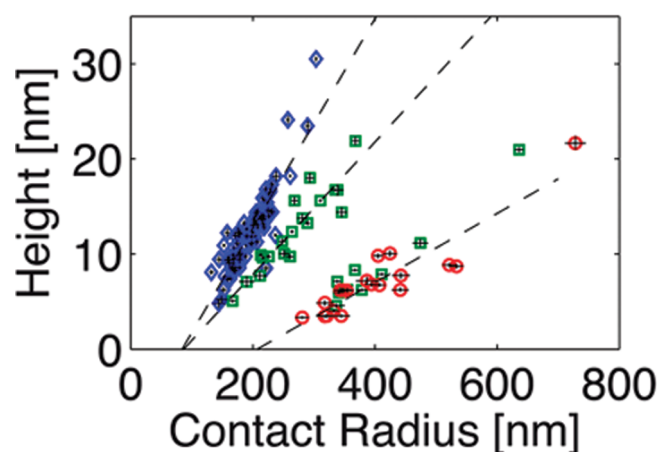


Figure 5. Spreading of particles on untreated silicon substrate upon 24 h of incubation. Blue diamonds indicate F_2 particles, green squares indicate F_1 particles, and red circles indicate F_0 particles. Error bars on the data points indicate 95% confidence intervals from the spherical cap fit used to obtain parameters. Dashed lines are linear fits of h versus a of the form $h = p_1 a + p_2$ with coefficients $p_1 = 0.036 \pm 0.008$, $p_2 = -7.52 \pm 3.41\text{ nm}$ (F_0), $p_1 = 0.069 \pm 0.015$, $p_2 = -5.84 \pm 4.17\text{ nm}$ (F_1), $p_1 = 0.11 \pm 0.013$, $p_2 = -9.30 \pm 2.61\text{ nm}$ (F_2). The subset of F_1 particles that show extensive spreading was omitted during the fit. The fitted parameters indicated $\pm 95\%$ confidence intervals.

The results are shown in Figure 5. Here, blue diamonds indicate F_2 particles (highly functionalized), green squares indicate F_1 particles (medium functionalized), and red circles indicate F_0 particles (not functionalized) (see Table 1). We found that the extent of spreading was highly dependent on the degree of functionalization, such that nonfunctionalized particles, F_0 , spread more extensively. The maximum height was in the range from 3 to 4 to 25 nm, while the contact radius ranged from 300 to 800 nm. The aspect ratio of the height to contact radius ranged from 1% to 3%, with the smallest particles having the lowest aspect ratio.

The most highly functionalized particles, F_2 , spread the least (blue diamonds in Figure 5). The height, h , was in the range of 5–30 nm, while the contact radius varied from 150 to 300 nm. Here the ratio h/a was in the range from 4 to 9%, and again the

smallest particles had a lower aspect ratio than the larger ones. The intermediately functionalized particles, F_1 , were generally spreading more than F_2 but less than F_0 particles. However, a subset of F_1 particles (7 out of 28) spread similarly to the F_0 particles. These particles were omitted from the linear fit.

For all particles, linear fits of h versus a intersected the positive x axis. This is consistent with the observed increase of the aspect ratio h/a as a function of the particle size and indicates that no single contact angle described the different particles. Rather, the contact angle depended on the size of the particle.

Thus, increased functionalization leads to less spreading. This appears to contradict the notion that spreading is aided by attractive interaction between the droplet and a surface mediated by specific chemical binding, such as silanization. However, as demonstrated in Figure 4, functionalization also increases the cohesive interactions in a polymer particle, which may counteract spreading. To further investigate the interplay of surface interactions and cohesive forces, we changed the surface energy by performing the corresponding studies with Me2-OdCS-treated surfaces, where the interactions of the functional groups on the polymer with the surface are modified.

3.2. Surface Properties of the Substrate Affect Spreading. We therefore modified the wetting properties of the substrate. This is expected to change the polymer–surface interactions without affecting the bulk properties of the polymer, giving insight into the balance of forces governing spreading. We therefore incubated the three different types of functionalized particles for 24 h at $T = 80\text{ }^{\circ}\text{C}$ on a Me2-OdCS-modified surface.

The results are shown in Figure 6. Here, green squares show the height and width of particles on the Me2-OdCS-modified substrate. Blue circles represent particles measured on an untreated substrate and are reproduced from Figure 5 for comparison. Particles with different functionalizations are plotted in separate panels: Figure 6A shows nonfunctionalized particles, F_0 , Figure 6B shows intermediately functionalized particles, F_1 , and Figure 6C shows the highly functionalized particles, F_2 . Dashed lines are linear fits of the height and width of groups of particles; fitting parameters including 95% confidence intervals are shown in the figure caption.

Nonfunctionalized particles spread less on the Me2-OdCS-treated surface, and the scaling between the height and width seemed qualitatively different from that on the untreated surface: The linear fit of h versus a intersected close to the origin of the axes, with the confidence interval containing the origin. This indicates that h was directly proportional to a and the aspect ratio, h/a , was largely independent of the particle size. On average, we found $\langle h/a \rangle = (3.9 \pm 0.12)\%$ ($\pm 95\%$ confidence interval, $N = 78$).

For the F_1 particles, the qualitative difference between treated and untreated surfaces was less because spreading on both substrates gave h/a depending on the particle size (Figure 6B). On the Me2-OdCS surface, we observed that the aspect ratio of the particles was in the range of 4.5–7%, depending on the particle size. However, overall the F_1 particles spread less on the Me2-OdCS-modified surface.

The spreading of the highly functionalized particles, F_2 , was also different depending on the surface properties, although the difference was much smaller than those for F_0 and F_1 (Figure 6C). Linear fits of h versus a showed a lower slope for F_2 particles on the Me2-OdCS-treated surface (slope = 0.088 ± 0.004) than on the untreated surface (slope = 0.110 ± 0.004). The intersect with the y axis was at $-4.4\text{ nm} \pm 1.8\text{ nm}$ on the treated surface compared to $-9.3\text{ nm} \pm 2.6\text{ nm}$ on the untreated surface. These differences were statistically significant (one-way ANCOVA: slopes, $p = 0.0078$; intersects, $p = 0.0038$).

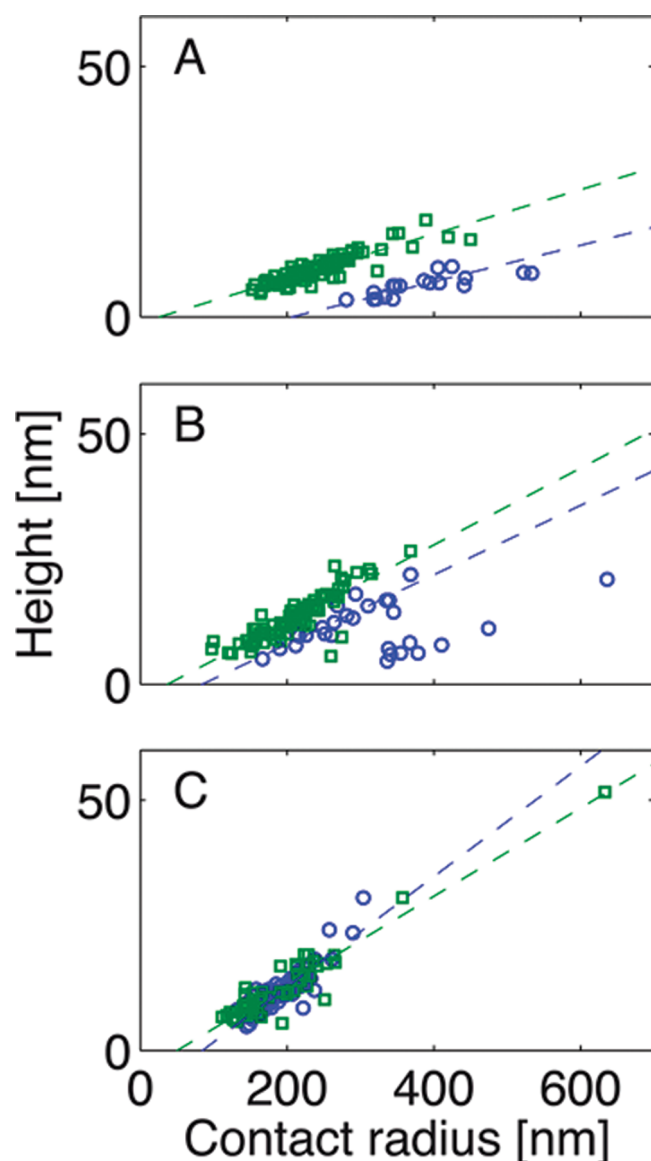


Figure 6. Analyses of the shape of functionalized polymer particles incubated 24 h at $T = 80\text{ }^{\circ}\text{C}$. Results for spreading on the Me2-OdCS-modified surface are shown in green. Results for the untreated surface are shown in blue and are reproduced from Figure 5. Panel A shows F_0 , panel B, F_1 , and panel C, F_2 . Error bars on the particles are similar to those in Figure 5 and omitted for clarity. Dashed lines are linear fits of h versus a of the form $h = p_1 a + p_2$ with coefficients $p_1 = 0.044 \pm 0.005$, $p_2 = -1.15 \pm 1.26\text{ nm}$ (F_0), $p_1 = 0.077 \pm 0.010$, $p_2 = -2.81 \pm 2.21\text{ nm}$ (F_1), and $p_1 = 0.088 \pm 0.009$, $p_2 = -4.41 \pm 1.81\text{ nm}$ (F_2). As in Figure 5, coefficients are given at $\pm 95\%$ confidence intervals and the subset of highly spreading particles is not included in the linear fit in panel B.

The observations shown in Figures 5 and 6 are interesting for several reasons. Most linear fits intersected the y axis below the origin (p_2 was statistically significantly less than 0). This means that under most conditions the particle height h was not directly proportional to a and therefore the contact angle was dependent on the particle size. The exception was F_0 particles on the Me2-OdCS-treated surface (Figure 5A, green squares), where the intersection with the y axis of the linear fit was close to the origin ($-1.2 \pm 1.5\text{ nm}$). For these particles, the ratio h/a was nearly constant as a function of the particle size and the variation in the

contact angle with the particle size smaller than that for F_0 particles on the untreated surface. For these particles, the average contact angle was $\langle\theta\rangle = 4.49 \pm 0.14^{\circ}$ ($N = 78$). We interpret this observation as the nonfunctionalized polymer partially wetting the Me2-OdCS surface, with $\langle\theta\rangle$ being close to θ_0 , the thermodynamic equilibrium contact angle for the polymer on this surface. The nonfunctionalized particles spread even more on the untreated surface. However, here h was not proportional to a and the contact angle varied with the particle size. We interpret this as an indication of a still ongoing spreading process at the time of measurement. Given the low h/a ratio, we find it likely that the nonfunctionalized polymer is wetting the untreated silicon substrate. Thus, on the Me2-OdCS substrate, the driving force for spreading must be lower than that on the untreated silicon substrate. We also expect the spreading force for the functionalized particles to be lower on the Me2-OdCS-treated surface because the base polymer is the same and its ability to form specific interactions is lower.

What then determines the height and width of the F_2 particles? One hypothesis could be that a balance of interior elasticity and spreading force determines the shape of the functionalized particles.⁹ However, if this were the case, F_2 particles would spread less on the Me2-OdCS surface because of the lower driving force. This is not what we observe in Figure 6C. Therefore, we find it more plausible that the F_2 particles reside in a quasistable nonequilibrium state where interactions between the polymer and substrate prevent further spreading.

3.3. Kinetics of Spreading Is a Two-Stage Process. Thus, interactions between the polymer and surface seem to halt the spreading. We then asked if this effect was a specific effect to the functional groups of the F_2 polymer or a generic feature of the spreading of nanoscale polymer droplets. In order to answer this question, we examined the time development of the particle morphology. We prepared samples of particles on untreated silicon substrates and examined the height and width of the particles at different time points during the spreading process. The samples were incubated at $80\text{ }^{\circ}\text{C}$. At specific times, the incubation was interrupted, the substrates were briefly transferred to the atomic force microscope, and the particle morphology was examined at room temperature. It was not possible to relocate exactly the same particles for measurements at different times so different representative ensembles were analyzed. The results for 24 h were from a different sample incubated without interruption; these data points are also shown in Figure 5.

The time development of the particle morphology is presented in Figure 7. Figure 7A shows functionalized particles of type F_2 . We found no substantial time evolution for these types of particles after 1 h of incubation. The result of a similar experiment conducted with F_0 particles is shown in Figure 7B. Remarkably, the distribution of h and a of the F_0 particles after 1 h of incubation was very similar to that of the F_2 particles (compare blue squares in Figure 7A,B or see Figure 9). However, in contrast to the F_2 particles, the shape of the F_0 particles continued to undergo a slow transition from a relatively high aspect ratio to increasingly flat particles. Furthermore, the relationship between h and a was nonlinear at intermediate incubation times (4 and 7 h). After 4 h, the conformational change was larger in small particles compared to large ones. After both 4 and 7 h, some particles seemed to have morphology similar to that after 1 h. After 24 h of incubation, all observed particles had spread.

At room temperature, substantial deformation of the particles also took place shortly after the sample was dry and ongoing deformations took place on a time scale of months (data not shown).

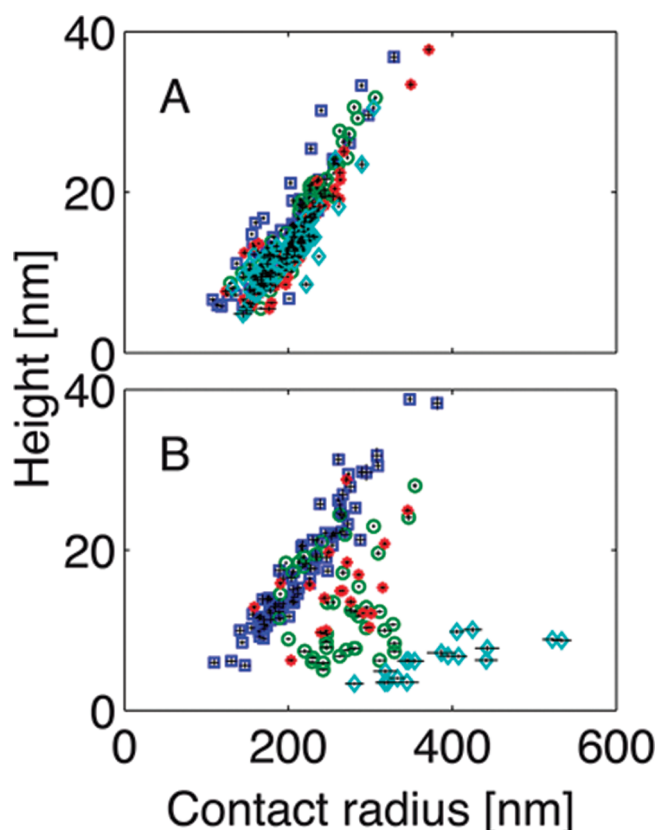


Figure 7. Time development of particles on hydrophilic silica, showing h as a function of a for particles after different incubation times at 80 °C. Blue squares indicate 1 h, green circles 4 h, red asterisks 7 h, and cyan diamonds 24 h. Panel A shows the results for F_2 particles and panel B those for F_0 particles. Data for 24 h are reproduced from Figure 5.

Thus, the spreading process seemed to include two stages: A fast stage occurs in which droplets deform on a fast time scale. This process is independent of functionalization. Then particles evolve on a subsequent slow nonlinear spreading process. This latter process is hindered by a high degree of functionalization.

4. DISCUSSION

We consider the spreading of functionalized polymer nanoparticles on silicon surfaces as a model system for interaction of latex particles to inorganic material in, for example, coatings. We investigated this system and compared it with a Me2-OdCS-modified substrate in order to identify key features of the adhesion process.

We interpret the spreading of the particles as a two-stage process. The first process brings the particles in less than 1 h (while incubated at $T = 80$ °C) into a state characterized by a size-dependent aspect ratio h/a (from ~ 5 to 10% for particles with a from 100 to 400 nm). The configuration after the fast process does not depend on functionalization (because the shapes of the F_0 and F_2 particles were similar after 1 h; Figure 7), but it seems to depend on the wetting properties of the substrate (because the shape of the F_2 particles depended on surface treatment; Figure 6C). At their first contact with the surface, the particles are spherical. Therefore, this first stage of the spreading covers the largest part of the deformation of the particles.

The second stage in the spreading process is slow and depends on the functionalization and wetting properties of the substrate.

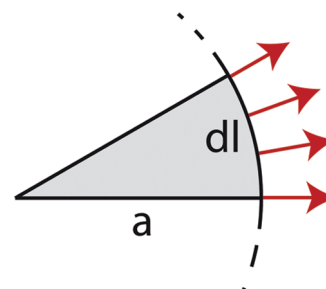


Figure 8. Small segment of the interface between the polymer and surface of the spherical cap of contact radius a . The segment is defined by the radius a and a small line segment of the perimeter of the drop. The arrows indicate the direction of the spreading force given by eq 3.

The highly functionalized particles (F_2) did not enter this phase at all on the time scale of this experiment (Figure 7A). For the nonfunctionalized particles (F_0), the spreading in this phase was substantially faster for small particles than for larger particles. It seemed that the intermediately functionalized particles were able to spread by this process, albeit at a slower pace.

What could be the origin of the fast process? In the spreading of macroscopic drops, an initial fast stage is often encountered.^{18,19} This is related to the inertia of the spreading liquid. However, in our case, the Reynolds number is very low, so inertial forces are irrelevant.²⁰ Instead, we look into the physical properties of the polymer and substrate for the origin of the fast spreading. There is evidence suggesting that the dynamics of thin polymer films are dominated by slippage.^{20,21} Furthermore, the radius of gyration of the vinyl acetate-co-ethylene copolymer used in this study is around 10 nm. This is estimated using the relation $R_g^2 = C_\infty N l^2 / 3$ for an unperturbed chain, with characteristic ratio $C_\infty = 8.79$,²² monomer length $l = 0.154$ nm, and degree of polymerization $N = M/M_{\text{rep}}$, where $M = 10^5$ is the molecular weight of the whole chain and $M_{\text{rep}} = 66$ is the molecular weight of the monomers. For the F_2 particles (the particles that spread the least), we found that h was similar to a few times R_g in the end configuration of the particles. The physical properties of the polymer films change when the film height and R_g are of similar magnitude^{23–27} because many of the polymers will have segments in contact with the surface. For large drops, this may only happen close to the edge of the droplet; for the nanoscale drops in the ensemble, this happens everywhere in the droplet.

We therefore consider our droplets as a special case of the two-fluid model proposed by Bruinsma²⁸ and propose that the initial fast phase of the spreading for the polymer droplets occurs via collective slip along the interface. Slippage is possible because of high stress at the interface during the initial stages of the spreading. As the spreading continues, the area of the interface increases and the contact angle becomes lower. Both processes lead to a reduction in the interface stress. We propose that the transition from the fast regime to the slow regime coincides with a transition from slippage to sticking (stick–slip transition) occurring when the interface stress falls below a critical value σ^* .^{29,30}

In the following, we shall derive scaling properties predicted by this model and use it to estimate the critical wall stress at which the stick–slip transition occurs. For simplicity, we describe the drop as a spherical cap with contact radius a and maximum height h . Let us consider a wedge of the circular interface between the drop and substrate, as shown in Figure 8. The wedge is defined by a small length dl along the perimeter

and the contact radius a . The area of the segment is $dA \approx a/2dl$. For a given contact angle θ , the driving force on the segment is given by an unbalanced Young force defined by the polymer surface tension γ and the equilibrium contact angle θ_0 .³¹ As argued above, the thermal equilibrium contact angle for the polymer droplets on the untreated surface is very low. Consequently, we set $\cos(\theta_0) = 1$. For small contact angles, the driving force may be approximated as

$$dF(\theta) = \gamma[1 - \cos(\theta)] dl \approx \frac{\gamma}{2} \theta^2 dl \quad (3)$$

where γ denotes the surface energy of the polymer–air interface.

We assume that the driving force is opposed by stationary friction at the interface. We are interested in the force required to halt advancement of the contact line a given stage of the spreading process. At a given contact area dA halting spreading requires an interface stress given as

$$\sigma da = \frac{\sigma a}{2} dl = dF(\theta) \quad (4)$$

In our stick-slip model the maximal possible value of σ is σ^* . If σ is larger than σ^* , the interface will yield. During the initial stages of the spreading, the driving force (eq 3) is high and the area of the interface is low. Therefore, $\sigma > \sigma^*$ and the interface yields. Consequently, the droplet spreads relatively fast. However, during this process, the driving force is continuously reduced and the contact area increases, leading to lower σ , the stress required to halt spreading. Ultimately $\sigma \approx \sigma^*$ and consequently spreading by slippage stops. The critical contact angle θ_{ss} at which the stick–slip transition occurs can be found by combining eqs 3 and 4. Inserting the critical stress σ^* , we get

$$\gamma \theta_{ss}^2 = \sigma^* a_{ss} \quad (5)$$

where a_{ss} is the contact radius at the stick–slip transition. Similarly, we define h_{ss} as the particle height at the stick–slip transition. Notice that θ_{ss} , a_{ss} , and h_{ss} depend on the size of the droplet, whereas σ^* is a constant depending on the polymer and substrate. Because $a \approx h$, we approximate

$$\theta \approx \sin(\theta) = \frac{2ah}{a^2 + h^2} \gg \frac{2h}{a} \quad (6)$$

which enables us to write a scaling relation between h_{ss} and a_{ss} , giving

$$4\gamma h_{ss}^2 = \sigma^* a_{ss}^3 \quad (7)$$

Alternatively, this equation can be used to determine the value of σ^* if h and a are both known. Equation 7 may be expressed as the scaling relation $h_{ss} \propto a_{ss}^{3/2}$.

The prediction of eq 7 is shown as the solid black line in Figure 9 and appears to be a reasonable description of the data. In the plot, we used $\gamma = 50 \text{ mJ/m}^2$ ⁹ and $\sigma^* = 6 \text{ kPa}$. Open symbols represent F_2 particles, while solid symbols are F_0 particles both after 1 h of incubation.

In another test, we treated the power law exponent as a fitting parameter. The fitted exponent was between 1.55 and 1.78 (95% confidence interval; Figure 9, green dashed line), close to the predicted value.

In macroscopic experiments, stick–slip transitions may occur at wall stresses from 1 kPa³² to 500 kPa,³³ consistent with our result. Our value, $\sigma^* = 6 \text{ kPa}$, falls on the low end of the regime. However, our assumption that the stress is equally distributed

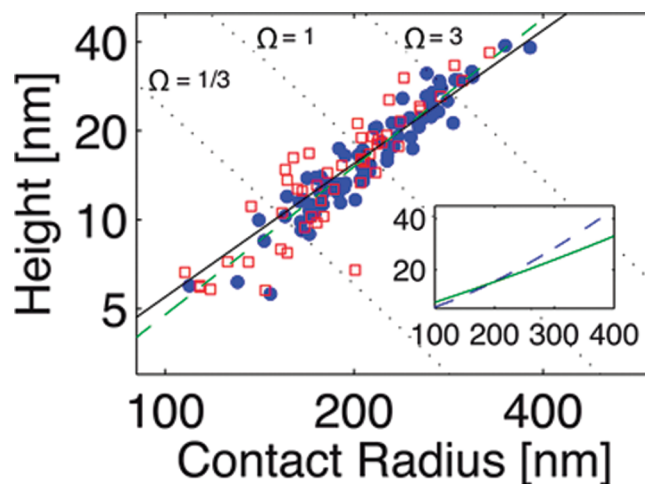


Figure 9. Open symbols indicate F_2 particles after 1 h of incubation (same data as those in Figure 7A). Filled symbols are F_0 after 1 h of incubation (same data as those in Figure 7B). The black line indicates a power law relationship $h \propto a^{3/2}$, as given by eq 7 using $\gamma_1 = 50 \text{ mJ/m}^2$ ⁹ and $\sigma^* = 6 \text{ kPa}$. The dashed green line is a power law fit, giving an exponent between 1.55 and 1.78 (95% confidence interval). The intersecting dotted lines indicate constant volume contours, corresponding to volumes of $1/3$, 1, and 3 times a typical particle with diameter 130 nm. The inset shows scaling relations obtained on different surfaces; see the text. The dashed line is eq 7; the solid line shows eq 8 with $\theta_0 = 4^\circ$ and $\sigma^* = 1 \text{ kPa}$.

over the entire surface area is likely to be an overestimation. The local stress may therefore be higher than 6 kPa, which here represents the surface average. Another difficulty in the comparison with macroscopic measurements is the difference in time scales between typical stick–slip experiments and spreading. The velocities encountered are different by many orders of magnitude. Therefore, a slip velocity on the order of 100 nm/h, which is the relevant scale in our AFM experiments, may not be observable in macroscopic experiments.

On the Me2-OdCS-treated surface, we expect the critical stress to be lower.³⁴ This will lead to continued spreading at lower contact angles. This, however, is compensated for by a higher contact angle, in our case around 4 – 5° . In order to analyze the results from the Me2-OdCS surface, we extended eq 7 to the case of partial wetting with equilibrium contact angle θ_0 :

$$h_{ss}^2 = \frac{\sigma^* a_{ss}^3}{4\gamma} + \theta_0^2 a_{ss}^2 \quad (8)$$

The inset of Figure 9 shows two different scaling relations between h and a . The dashed line is the result for complete wetting (eq 7) using $\sigma^* = 6 \text{ kPa}$. The solid line shows the result of eq 8 using lower critical stress $\sigma^* = 1 \text{ kPa}$ and equilibrium contact angle $\theta_0 = 4^\circ$. Comparing with Figure 6C, we conclude that our slip model of the spreading is also consistent with the data in the partial wetting regime on the Me2-OdCS-treated surfaces.

What happens in the slow phase of spreading? The spreading in this phase was highly modulated by functionalization: No spreading of the highly functionalized F_2 particles was detected, the F_1 particles spread somewhat, and finally F_0 particles continued to evolve over a time span of at least 24 h. The evolution passed through regimes with nonlinear relationships between a and h .

Because the height of the particles was less than R_g , the spreading mechanism in the slow regime must still involve movements of the polymer segments over the polymer–substrate interface. Two

mechanisms could be at play. The movement of the contact line may be dominated by small movements of individual chain segments. In this picture, the inability of F_2 particles to spread can be due to a combination of specific chemical interactions between the functional groups and substrate and internal cross-linking. For nonfunctionalized particles, this mode of spreading will lead to a slow creeping contact line.

An alternative mechanism could be a continuation of the stick–slip mechanism after relaxation of internal stresses. As mentioned above, the local stress at the interface may be higher than σ^* . However, immediately after termination of the fast phase, such regions may be prevented from spreading further by internal stresses in the polymer droplet. As these relax on a slow time scale, slippage may occur in parts of the polymer drop. The time scale between stick and slip is determined by the relaxation time of the polymer. According to Figure 4, this time scale is longer for F_1 particles compared to F_0 particles. In addition, there will be no relaxation in F_2 particles. In the stick–slip picture, the inability of the F_2 particles to spread is due to the rubberlike rheological properties. With the local stick–slip mechanism, specific substrate interactions could, in principle, also contribute and hinder spreading. However, on the Me2–OdCS surface, functionalized particles (both F_1 and F_2) spread less than the nonfunctionalized particles even though surface interactions are bypassed. Therefore, it is tempting to conclude that specific interactions with the substrate play a minor role in the phase of slow spreading. However, specific substrate interactions may still contribute to the spreading kinetics by increasing the internal relaxation time. For nonfunctionalized particles, the stick–slip picture will cause the contact line to move through sudden fast phases until the stress at the interface again is less than σ^* .

The time resolution in the present measurements does not allow us to measure the spreading velocity directly. However, the morphology of highly spreading particles deviated significantly from a spherical cap (Figures 2D and 3). Thus, in these cases, the movement of the contact line was faster than the time scale of equilibrating the polymer–air interface. These deviations from the spherical cap indicate that regions of the polymer droplet were spreading at a higher pace than the rest. Therefore, we find it likely that spreading during the slow phase is a stick–slip process, where parts of the droplet move in competition with the internal stress.

5. CONCLUSION

We investigated the spreading of functionalized polymer particles and found that the kinetics of the spreading was in two phases. The first phase was short (≤ 1 h at $T = 80$ °C), covered the largest part of the spreading. The shape of the particles after this phase was not dependent on functionalization. During the second phase, spreading was slower and evolved on a longer time scale (≥ 24 h at $T = 80$ °C). The ability to spread in this phase was strongly dependent on functionalization.

We propose that the spreading proceeds as a slip process. In the fast phase, a large fraction of the polymer droplet moves as an entity across the interface. After the fast phase, we observed particle morphology consistent with a transition from slip to stick occurring at a critical shear stress of $\sigma^* = 6$ kPa. This stick–slip transition implies a scaling relationship between the height and width, where $h \sim a^{3/2}$. In the slow phase, the driving force for spreading is insufficient to make all polymer segments slip.

Instead, we propose a mechanism where small regions of the drop can slip after relaxation of internal stresses. Therefore, spreading in this phase becomes dependent on the rheological properties.

■ ASSOCIATED CONTENT

S Supporting Information. Particle size distributions of lattices as determined by light scattering (Figure 1), information about coverage of Me2–OdCS-treated surfaces (Figure 2), and further tests of AFM measurement (Figure 3). This material is available free of charge via the Internet at <http://pubs.acs.org>.

■ AUTHOR INFORMATION

Corresponding Author

*Present address: Department of Neuroscience and Pharmacology, Copenhagen University, Blegdamsvej 3B, DK-2200 Copenhagen N, Denmark. E-mail: jakobdr@sund.ku.dk.

■ ACKNOWLEDGMENT

VINNOVA and the industry-sponsored Centre for Amphiphilic Polymers are gratefully acknowledged for financial support. We also thank Celanese Emulsions Norden AB, Perstorp, Sweden, for kindly providing model latex dispersions and Daniela Bach for her assistance with the rheology experiment.

■ REFERENCES

- (1) Lin, F.; Meier, D. J. *Langmuir* **1995**, *11*, 2726–2733.
- (2) Ihalainen, P.; Backfolk, K.; Sirvio, P.; Peltonen, J. *Colloids Surf., A* **2010**, *354*, 320–330.
- (3) Routh, A. F.; Russel, W. B. *Langmuir* **1999**, *15*, 7762–7773.
- (4) Unertl, W. N. *Langmuir* **1998**, *14*, 2201–2207.
- (5) Touaiti, F.; Alam, P.; Toivakka, M.; Bousfield, D. W. *Mater. Sci. Eng., A* **2010**, *527*, 2363–2369.
- (6) Aradian, A.; Raphael, E.; de Gennes, P. G. *Macromolecules* **2002**, *35*, 4036–4043.
- (7) Granier, V.; Sartre, A. *Langmuir* **1995**, *11*, 2179–2186.
- (8) Israelachvili, J. *Intermolecular and Surface Forces*, 2nd ed.; Academic Press: London, 1992.
- (9) Lau, A. W. C.; Portigliatti, M.; Raphael, E.; Leger, L. *Europhys. Lett.* **2002**, *60*, 717–723.
- (10) Engqvist, C.; Forsberg, S.; Norgren, M.; Edlund, H.; Andreasson, B.; Karlsson, O. *Colloids Surf., A* **2007**, *302*, 197–203.
- (11) Stark, K.; Tschirner, P.; Ball, P.; Bueppelmann, K.; Kotschi, U.; Bueppelmann, K. U.S. Patent 6,624,243, 2003.
- (12) Massingill, J. L., Jr.; Bauer, R. S. In *Applied Polymer Science: 21st Century*, 1st ed.; Craver, C., Carraher, C., Eds.; Elsevier Science Ltd.: Oxford, U.K., 2000; pp 393–424.
- (13) Schantz, S.; Carlsson, H. T.; Andersson, T.; Erkselius, S.; Larsson, A.; Karlsson, O. J. *Langmuir* **2007**, *23*, 3590–3602.
- (14) Fadeev, A. Y.; McCarthy, T. J. *Langmuir* **2000**, *16*, 7268–7274.
- (15) Deegan, R. D.; Bakajin, O.; Dupont, T. F.; Huber, G.; Nagel, S. R.; Witten, T. A. *Nature* **1997**, *389*, 827–829.
- (16) de Gennes, P. G. *Rev. Mod. Phys.* **1985**, *57*, 827–863.
- (17) Williams, M. L.; Landel, R. F.; Ferry, J. D. *J. Am. Chem. Soc.* **1955**, *77*, 3701–3707.
- (18) Biance, A. L.; Clanet, C.; Quere, D. *Phys. Rev. E* **2004**, *69*.
- (19) Bird, J. C.; Mandre, S.; Stone, H. A. *Phys. Rev. Lett.* **2008**, *100*.
- (20) Baumchen, O.; Jacobs, K. J. *Phys.: Condens. Matter* **2010**, *22*.
- (21) Redon, C.; Brzoska, J. B.; Brochardwyart, F. *Macromolecules* **1994**, *27*, 468–471.
- (22) Tyagi, M.; Arbe, A.; Alegria, A.; Colmenero, J.; Frick, B. *Macromolecules* **2007**, *40*, 4568–4577.

- (23) Hirz, S.; Subbotin, A.; Frank, C.; Hadziioannou, G. *Macromolecules* **1996**, *29*, 3970–3974.
- (24) Herminghaus, S.; Jacobs, K.; Seemann, R. *Eur. Phys. J. E* **2003**, *12*, 101–110.
- (25) Li, C. H.; Kim, H. J.; Jiang, J.; Li, C.; Koga, T.; Lurio, L.; Schwarz, S.; Narayanan, S.; Lee, H. J.; Lee, Y. J.; Jiang, Z.; Sinha, S.; Rafailovich, M. H.; Sokolov, J. C. *Europhys. Lett.* **2006**, *73*, 899–905.
- (26) Israelachvili, J.; Luengo, G.; Schmitt, F. J. *Abstr. Pap. Am. Chem. Soc.* **1996**, *212*, 104–PMSE.
- (27) Subbotin, A.; Semenov, A.; Hadziioannou, G.; ten Brinke, G. *Macromolecules* **1996**, *29*, 1296–1304.
- (28) Bruinsma, R. *Macromolecules* **1990**, *23*, 276–280.
- (29) Boukany, P. E.; Tapadia, P.; Wang, S. Q. *J. Rheol.* **2006**, *50*, 641–654.
- (30) Brochard, F.; Degennes, P. G. *Langmuir* **1992**, *8*, 3033–3037.
- (31) Brochardwyart, F.; Degennes, P. G. *Adv. Colloid Interface Sci.* **1992**, *39*, 1–11.
- (32) Inn, Y. W.; Wang, S. Q. *Phys. Rev. Lett.* **1996**, *76*, 467–470.
- (33) Leger, L.; Hervet, H.; Charitat, T.; Koutsos, V. *Adv. Colloid Interface Sci.* **2001**, *94*, 39–52.
- (34) Wang, S. Q.; Drda, P. A. *Rheol. Acta* **1997**, *36*, 128–134.